Electronic structure evolution of the magnetic Weyl semimetal Co₃Sn₂S₂ with hole and electron doping

Himanshu lohani [1], Paul Foulquier,[1] Patrick Le Fèvre,[2] François Bertran,[2] Dorothée Colson,[3] Anne Forget [3], and Véronique Brouet[1]

[1]*Université Paris-Saclay, CNRS, Laboratoire de Physique des Solides, 91405, Orsay, France*
[2]*Synchrotron SOLEIL, L'Orme des Merisiers, Saint-Aubin-BP 48, 91192 Gif sur Yvette, France*
[3]*Université Paris-Saclay, CEA, CNRS, SPEC, 91191 Gif-sur-Yvette, France*

Co₃Sn₂S₂ has been established as a prototype of a magnetic Weyl semimetal, exhibiting a giant anomalous Hall effect in its ferromagnetic phase. An attractive feature of this material is that Weyl points lie close to the Fermi level, so one can expect a high reactivity of the topological properties to hole or electron doping. We present here a direct observation with angle-resolved photoemission spectroscopy of the evolution of the electronic structure under different types of substitutions: In for Sn (hole doping outside the kagome Co plane), Fe for Co (hole doping inside the kagome Co plane), and Ni for Co (electron doping inside the kagome Co plane). We observe clear shifts of selected bands, which are due both to doping and to the reduction of the magnetic splitting by doping. We discriminate between the two by studying the temperature evolution from a ferromagnetic to paramagnetic state. We discuss these shifts with the help of density-functional theory calculations using the virtual crystal approximation. We find that these calculations reproduce rather well the evolution with In, but largely fail to capture the effect of Fe and Ni, where local behavior at the impurity site plays an important role.

I. INTRODUCTION

Topological quantum materials have become a core area of research in the field of condensed matter physics in the past decade. Weyl semimetals (WSMs) form a part of this broad area of research. They feature inverted bands between which a gap closes at only a few nondegenerate Weyl points (WPs). These points act as sources or sinks of Berry flux, giving rise to magnetoelectric effects, such as the chiral anomaly [1]. They can be formed either by breaking the inversion symmetry (IS) or the time reversal symmetry (TRS). The best known examples of WSMs are due to IS breaking, as studied in TaS [2], TaP [3], and TaIrTe4 [4]. There are fewer examples of TRS broken WSMs, as they inherently display strong electronic correlations, which are more difficult to control.

Recently, Co₃Sn₂S₂ has been identified as a prototype example of a magnetic WSM [5]. It has a rhombohedral structure, where Co atoms form a kagome pattern layer. Below the Curie temperature of ∼177 K [5], the Cobalt atoms host local moments $M = 0.3 \ \mu_B$, which are ferromagnetically aligned along the c direction [6]. More complex helimagnetic and antiferromagnetic phases have been suggested to form with doping [7]. Despite the rather small value of the magnetic moment, a record value of the anomalous Hall conductivity (AHC) has been measured by Liu *et al.* [5], which is considered evidence of the strong Berry curvature around the WPs contributing significantly to the AHC [8,9]. Subsequently, angle-resolved photoelectron spectroscopy (ARPES) has mapped linearly dispersive bulk Weyl bands crossing just above the Fermi level (E_F) [10,11], in fair agreement with

density-functional theory (DFT) band-structure calculations [12,13]. Moreover, they observed surface states, which could form Fermi arcs between the WPs, although there remain discrepancies between the reports about which of these surface states are topological [10,14]. Above T_C, a ∼100 meV shift of the bulk bands has been observed [14,15], with the surface states either vanishing [14] or smoothly evolving to Z₂-type surface states [15].

An attractive feature of Co₃Sn₂S₂ is that WPs lie only ∼60 meV above E_F. Therefore, attempts have been made to tune the E_F position by changing the chemical potential by hole- and electronlike doping for fundamental study and applications [8,16–18]. For doping, Co and Sn are two suitable substitution sites in Co₃Sn₂S₂. When cobalt (atomic No. 27) is replaced by Fe (atomic No. 26) or nickel (atomic No. 28), one can expect a hole- and electronlike doping, respectively. However, these modifications take place directly in the active kagome Co plane and they may modify more deeply the electronic structure. On the other hand, substitution of In (atomic No. 49) at the Sn (atomic No, 50) site provides another way to add holes in the system. Although there are two Sn sites inside and outside the kagome planes, In was found to substitute preferentially at the interlayer position [19].

Earlier experiments have shown that the T_c of Co₃Sn₂S₂ decreases by In [8,24], Fe [17,20], and Ni [18,21] dopings. The AHC exhibits a nonlinear change, i.e., it first increases at small doping and then decreases very fast at larger doping. The role of intrinsic [8] and extrinsic [17] contributions in these evolutions have been discussed. Some evidence of a local moment behavior at the dopant site has been reported, either by the observation with STM of a localized bound

state at the In site [22] or by the appearance of a Kondo-like upturn below 50 K in the resistivity of Fe-doped samples [17], which is absent for In doping [8]. Therefore, it remains to be understood to what amount the role of substitutions can be regarded as a simple doping effect or a larger perturbation. Will there be a simple rigidlike shift of the electronic structure ? Will it be similar below and above T_c?

In this paper, we present direct observation with ARPES of the electronic band structure evolution of $Co_3Sn_2S_2$ doped by In, Fe, and Ni. We try to correlate these changes with changes in the magnetic moment by also studying the temperature dependence of the electronic structure. We compare our results with those of DFT-based first-principles calculations using the virtual crystal approximation (VCA) method [23] to mimic the doping effect. For clarity, we choose significantly doped samples, i.e., $x = 0.44$ for In ($Co_3Sn_{1.56}In_{0.44}S_2$), $x = 0.42$ for Fe ($Co_{2.58}Fe_{0.42}Sn_2S_2$), and $x = 0.6$ for Ni ($Co_{2.4}Ni_{0.6}Sn_2S_2$) for our study. We find that, as a first approximation, the evolution of the band structure can be described by a rigidlike shift, although the shift is different for Fe and In despite a similar hole doping value. For Ni doping, we observe previously unoccupied, electron pockets appearing near E_F. With our temperature-dependent study, we separate the amount of shift due to doping from the one due to magnetism.

II. EXPERIMENTAL DETAILS

We have grown single crystals of $Co_3Sn_2S_2$ and its doped compounds $Co_3Sn_{1.56}In_{0.44}S_2$, $Co_{2.58}Fe_{0.42}Sn_2S_2$, and $Co_{2.4}Ni_{0.6}Sn_2S_2$ by using Sn flux method, as reported before [5]. We checked crystallinity and stoichiometry of the samples by using XRD and energy dispersive x-ray measurements. Magnetic properties were measured by the Quantum Design SQUID system. Photoemission experiments were performed CASSIOPEE-B-ARPES beamline at SOLEIL synchrotron, using a SCIENTA-R4000 electron analyzer, where a liquid He-based cryostat was used to control the sample temperature. The samples were cleaved *in situ* and measured under ultrahigh vacuum condition at base pressure $\sim 5.0 \times 10^{-11}$ mbar. The resolution was ~ 15 meV and $0.2°$ for energy and momentum, respectively.

We perform density functional calculations for $Co_3Sn_2S_2$ by using the WIEN2K code [25] with the experimentally determined structure of $Co_3Sn_2S_2$. We estimate the effect of doping using the VCA approximation at the Co site and neglecting structural changes.

III. MAGNETIC PROPERTIES

Figures 1(a)–1(d) show magnetization as a function of temperature in $Co_3Sn_2S_2$, $Co_3Sn_{1.56}In_{0.44}S_2$, $Co_{2.58}Fe_{0.42}Sn_2S_2$, and $Co_{2.4}Ni_{0.6}Sn_2S_2$ collected in field cooled conditions at the external field value of 1000 Oe. The external field was parallel to the *c* axis of the crystals during the measurements. The magnetic moment rises sharply in all the samples indicating their ferromagnetic character, which is further confirmed by their ferromagnet hysteresis loop observed in the magnetic moment versus external field measurement at 10 K shown in Figs. 1(e)–1(h).

We estimate ferromagnetic transition (T_c) by using derivative plot (dM/dT versus T) and find that the T_c of the pristine compound goes down by all types of doping. It is 177K, 140 K, 118 K, and 20 K for pristine, Fe, In, and Ni doping. Similarly, the magnetic moment per Cobalt atom obtained from the saturation value of the magnetic moment from the hysteresis curves decreases. It is 0.33, 0.22, 0.15, and 0.04 μ_B for pristine, Fe, In, and Ni doping. Figure 1(i) shows that there is a nearly linear relation between T_c and the saturated magnetic moment. On the other hand, the coercive field (H_c) decreases by In and Fe doping but it increases in Ni doped samples as depicted in Fig. 1(j).

In a simple reasoning based on the number of available electrons, we expect nearly similar hole dopings for Fe and In ($x = 0.42$ and $x = 0.44$, respectively) and an electron doping $x = 0.6$ for Ni. A change of the total number of electrons can be simulated in a DFT calculation by the VCA method, where the average number of available electrons is assumed for all Co. In Fig. 1(k), we compare the magnetic moment per cobalt atom calculated as a function of doping concentration x by using VCA calculation to the experimental values. As shown in previous reports [9], for the pristine compound, the DFT calculation captures rather well the experimental moment, although it is slightly overestimated. $Co_3Sn_2S_2$ is a half metal and the near E_F DOS is composed of Co-3d states, which acquire spin-up polarized character in the ferromagnetic state. In the VCA approach, the moment is simply proportional to the number of electrons filling these states, therefore it increases linearly with the electron filling and keeps increasing from the hole to the electron doped side. However, in the electron-doped compound $Co_{2.4}Ni_{0.6}Sn_2S_2$ the magnetic moment is only 17% of the value of pristine compound, which is quite contrary to this prediction. This clearly shows that this VCA approach is insufficient to treat the effect of doping associated with Co/Ni substitutions. Indeed, DFT calculation using a supercell approach [18,21] predicts the decrease of magnetic moment, associated with the disorder introduced by Ni. Furthermore, Ni and Co in the kagome plane hold quite different magnetic moments in these calculations, emphasizing that they cannot be treated as a single average atom.

Interestingly, the calculated value with VCA for $x = 0.4$ (65% of its value in pristine compound) is rather close to the one found for In doping, where the magnetic moment decreases to $\sim 57\%$. This suggests that for substitutions outside the Co network, a simple charge transfer can be assumed. On the contrary, the magnetic moment found in our experiment for Fe is somewhat higher (77%), suggesting that dopings from Fe and In substitutions are quite different. Earlier report by Kassem *et al.* [24] have suggested that T_c decreases identically by Fe and In doping, which they considered as a proof of a similar effect of the two types of doping. While the nearly similar change in T_c could be consistent with our findings, we observe that the change in the magnetic moment is relatively larger. As doping is an important knob to tune the topological properties of $Co_3Sn_2S_2$, it is important to understand better how the electronic structure is modified by the different types of substitutions and particularly potential deviations from the rigid band filling picture. We will show that these substitutions indeed have a different impact on the electronic structure.
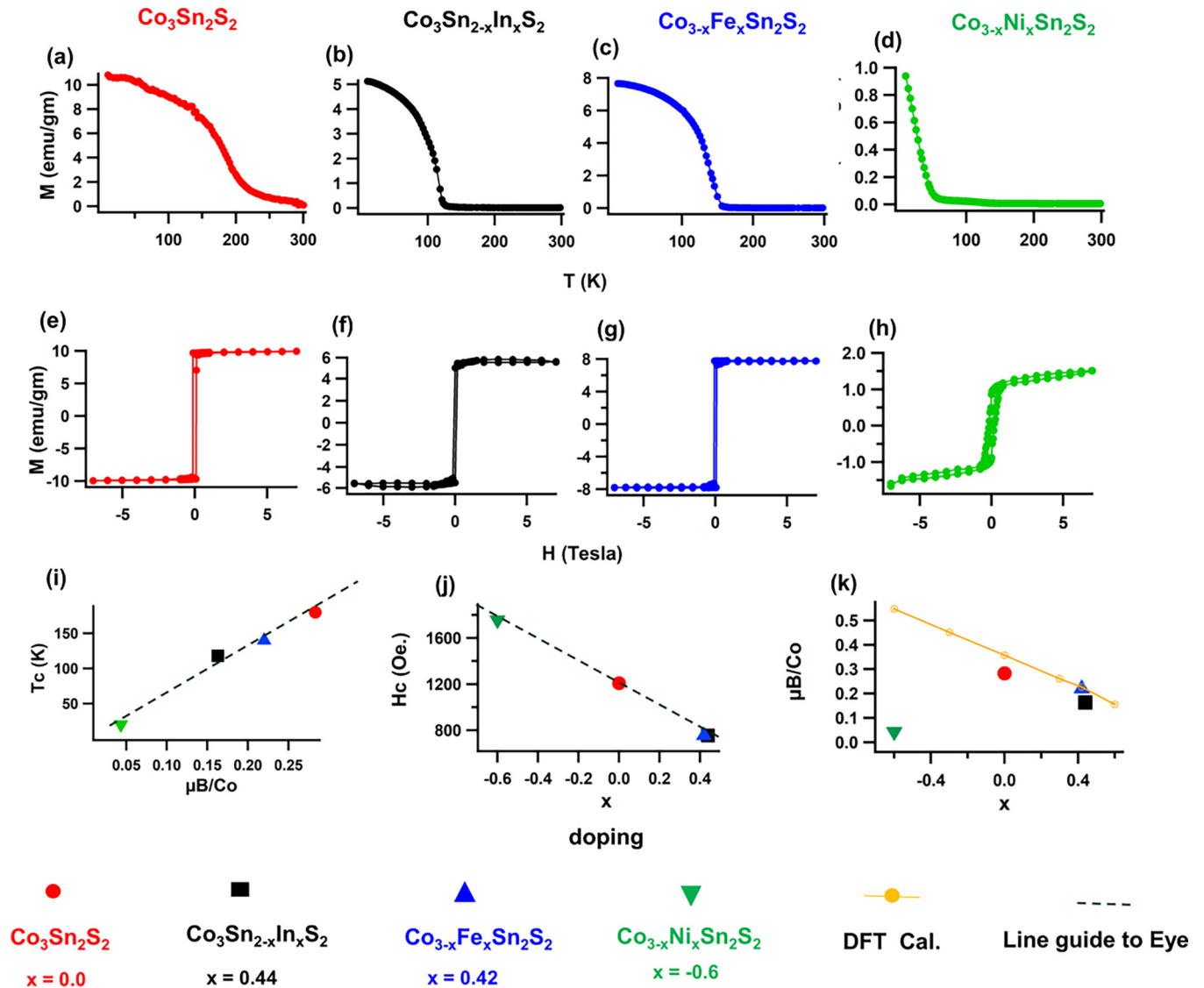
FIG. 1. M versis T plot at external field value of 1000 Oe for $Co_3Sn_2S_2$ (a) $Co_3Sn_{1.56}In_{0.44}S_2$ (b), $Co_{2.58}Fe_{0.42}Sn_2S_2$ (c), and $Co_{2.4}Ni_{0.6}Sn_2S_2$ (d). M versus H plot at temperature 10 K for $Co_3Sn_2S_2$, (e), $Co_3Sn_{1.56}In_{0.44}S_2$ (f), $Co_{2.58}Fe_{0.42}Sn_2S_2$ (g), and $Co_{2.4}Ni_{0.6}Sn_2S_2$ (h). (i) Curie temperature versus magnetic moment per Cobalt atom. (j) Coercive field as a function of doping concentration x, where $x = 0.0$, 0.42, 0.44, and -0.6 corresponds to $Co_3Sn_2S_2$ (red circle), $Co_3Sn_{1.56}In_{0.44}S_2$ (black square), $Co_{2.58}Fe_{0.42}Sn_2S_2$ (blue up triangle), and $Co_{2.4}Ni_{0.6}Sn_2S_2$ (green down triangle), respectively. (k) Magnetic moment as a function of doping concentration x. DFT predicted value of magnetic moment of $Co_3Sn_2S_2$ for hole- ($x > 0$) and electronlike ($x < 0$) doping is drawn in (k) by yellow color line. Black color dotted lines in (i) and (j) are guides to eye for the linear decrement.

IV. ELECTRONIC BAND STRUCTURE IN FERROMAGNETIC STATE

We start our investigation by comparing the electronic structure at low temperatures among the four compounds. Figures 2(a)–2(d) present Fermi surfaces (FSs) taken at 30 K by ARPES with a photon energy of 117 eV and linear horizontal (LH) light polarization. In photoemission, the momentum perpendicular to the in-plane direction (k_z) depends on the incident photon energy. We mapped the k_z dispersion of bands in $Co_3Sn_2S_2$ (see Appendix) and find that this photon energy of 117 eV corresponds to $k_z \simeq 0$, in agreement with previous reports of the literature[10]. In all the FS, a similar pattern can be observed, with high intensity spots along the Γ-K direction and slightly above the M point. For clarity, we

use here a 2D Brillouin zone (BZ); more details are given in Appendix B.

For quantitative comparison of the band structure of the various dopings, we choose three representative cuts in the FSs, through the high symmetry direction Γ - K - M in first BZ (cut#1), through the high intensity point above M at $k_y \simeq 0.85$ Å^{-1} (cut No. 2) and through Γ-K-M in second BZ (cut #3, this corresponds to $k_z = 2/3$, see Appendix B). In Appendix B, we give for reference the full electronic structure calculated by DFT along each cut. ARPES images taken along these different cuts are presented in Fig. 2. In each case, we identify a similar structure, but with a shift that is doping dependent. Along cut No. 1 [Figs. 2(e)–2(h)], the band structure in these experimental conditions is characterized by an electronlike band around Γ that we call δ (black line)
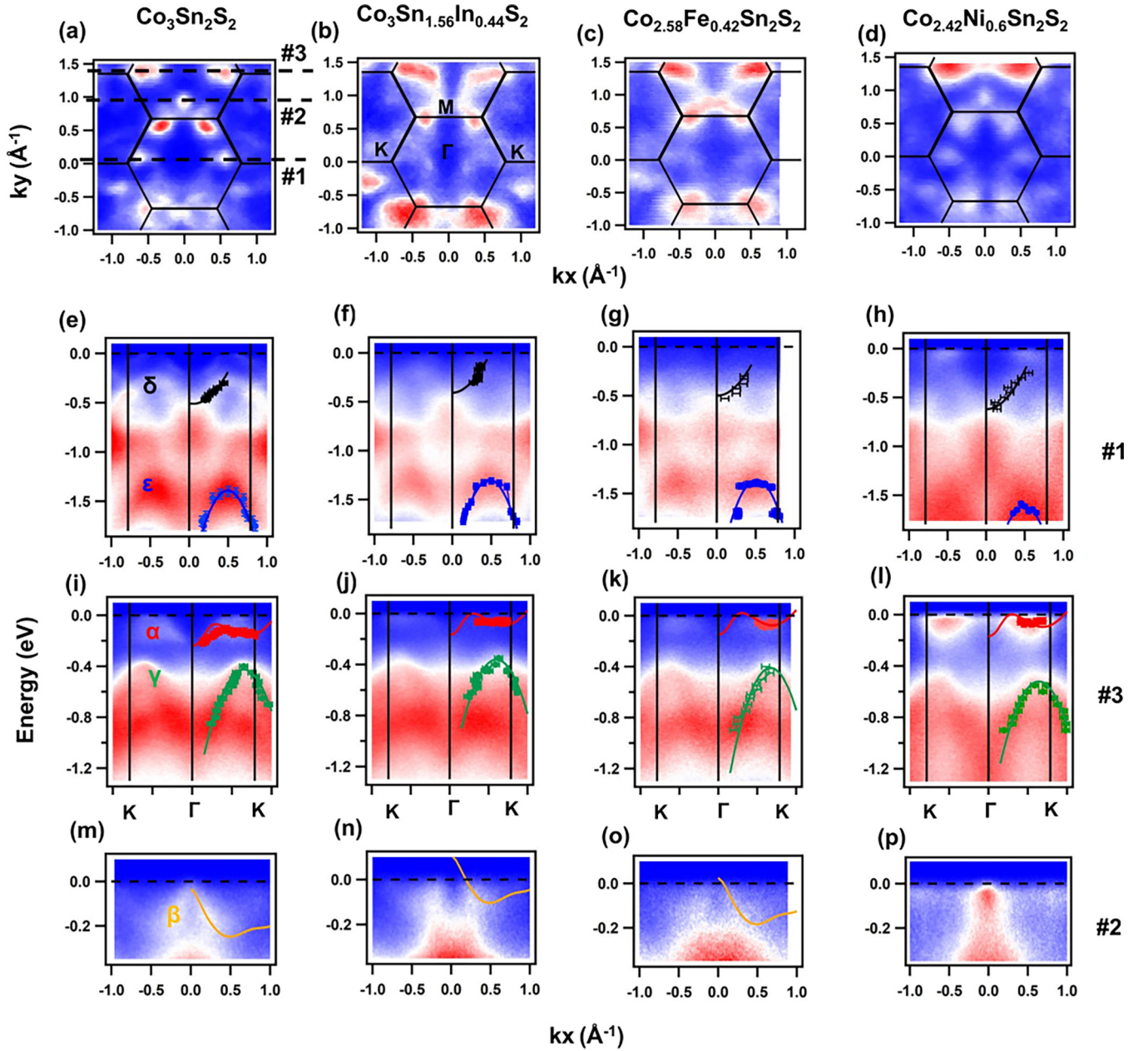
FIG. 2. (a)–(d) FS of $Co_3Sn_2S_2$, $Co_3Sn_{1.56}In_{0.44}S_2$, $Co_{2.58}Fe_{0.42}Sn_2S_2$, and $Co_{2.4}Ni_{0.6}Sn_2S_2$, respectively, collected at 30 K by using 117 eV LH polarized light. Black lines indicate the 2D hexagonal BZ (see Appendix B for more details). (e)–(h), (i)–(l), and (m)–(p) ARPES images of the above compounds along the cuts indicated in (a): cut No. 1 ($k_y \simeq 0$), No. 3 ($k_y \simeq 1.35$), and No. 2 ($k_y \simeq 0.85$ Å^{-1}), respectively. α, β, γ, δ, and ϵ bands are identified and marked by red, orange, green, black, and blue colours respectively. A parabolic fit is used for the γ, δ, and ϵ bands and a DFT model for α and β (see Appendix B). The DFT calculated bands are renormalized by a factor of 1.4 to match the experimental results.

and an intense parabolic patch at higher binding energy (BE) that we call ϵ (blue line). Along cut No. 3 [Figs. 2(i)–2(l)], one band (α, red) is identified near E_F and a broad intensity patch (γ, green) lies at higher BE. Finally, along cut No. 2 [Figs. 2(m)–2(o)], a clearly dispersing band (β, orange) is visible and crosses E_F with nearly linear dispersion. As will be justified later, this point is close to the Weyl crossing loop. This β band is superimposed to an electronlike band, which is possibly a surface state (it is more clearly visible in circular polarization, see Appendix C).

To track the position of these bands, we extract data points either by fitting the momentum dispersion curves (MDCs) to Lorentzian peaks or by taking the maxima of energy dispersion curves on flat parts of the dispersion where MDC peaks are unresolved. The γ, δ, and ϵ points are fitted to parabolic dispersion to estimate their extreme position. The near E_F bands α and β have more complicated shapes, which are well captured by DFT calculations for the pristine compound after using a renormalization factor of 1.4, as detailed in Appendix B and in agreement with previous reports [10,14].
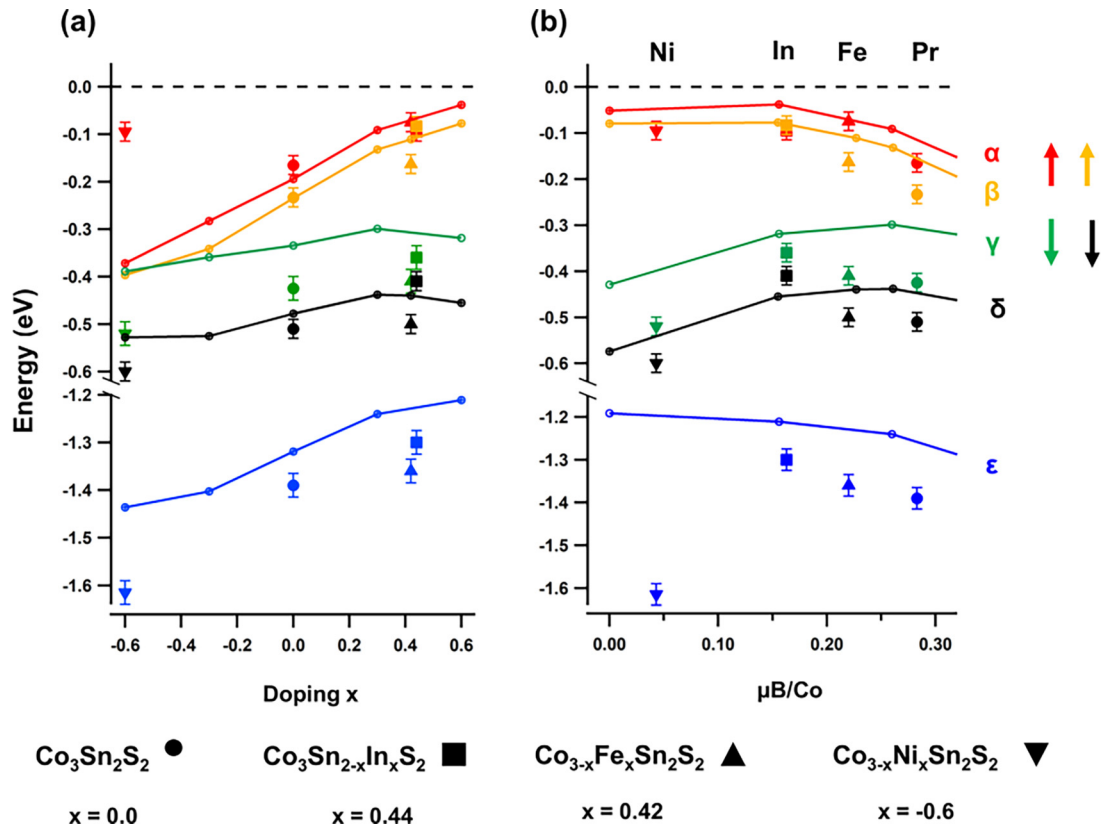
FIG. 3. Position of the α (red), β (orange), γ (green), δ (black), and ϵ (blue) bands defined in Fig. 2 with respect to (a) doping [hole (x > 0) and electron (x < 0)] and (b) magnetic moment per Cobalt atom. The solid lines correspond to the DFT-predicted doping-dependent change in the respective bands calculated using the VCA approximation [in (b), the positions for a doping corresponding to the given magnetic moment is used]. The position for γ, δ, and ϵ are defined at their extrema and for α and β at special k-points (see Appendix D).

We use these DFT bands as a model and shift them to match with the α and β bands in doped compounds. For Ni [Fig. 2(p)], it is not possible to describe the β band by such a rigid shift. A new electron pocket appears near E_F, presumably from a previously unoccupied band.

In Fig. 3, we summarize the evolution of the position of each band in the different compounds. We indicate the position of the bottom of the parabola for δ, the top of the parabola for γ and ϵ. For α and β bands, we use the position of the DFT model at $k_x = 0.51$ Å^{-1} and $k_x = 0.35$ Å^{-1}, respectively (see Appendix D). In Fig. 3(a), we plot these values as a function of the doping expected in case of complete charge transfer, e.g., a hole concentration with $x = 0.44$ for $Co_3Sn_{1.56}In_{0.44}S_2$, $x = 0.42$ for $Co_{2.58}Fe_{0.42}Sn_2S_2$, and an electron concentration $x = -0.6$ for $Co_{2.4}Ni_{0.6}Sn_2S_2$. We compare these evolutions with those expected for the DFT bands in the VCA calculation (solid lines). They shift almost linearly with doping, albeit with a different slope for spin up (α, β, and ϵ) and spin down (γ and δ). The calculated shifts match rather well with the observed ones on the hole-doped side, although it is systematically reduced in Fe (up triangles) compared to In (squares). The position of Fe is usually found halfway between those of the pristine compound and the one of In, as if the effective doping was closer to $x = 0.2$. For Ni, the shift of the spin-up band α is opposite to what would be expected for electron doping and strongly deviates from the VCA curve. On the other hand, the position of the spin-down

bands (γ and δ) and ϵ at high BE are consistent with electron doping and the calculated values, within experimental accuracy. This problem arises because the magnetic splitting is overestimated for Ni by the VCA calculation [see Fig. 1(k)].

Indeed, as is clear from Fig. 1, doping also modifies the magnetic properties of $Co_3Sn_2S_2$, which of course will affect the position of the bands in the magnetic state. Therefore, we replot in Fig. 3(b) the position of the bands with respect to magnetic moment, together with the position of the DFT bands at the VCA doping giving rise to this magnetic moment. The DFT-predicted spin-up (α, β, and ϵ) and spin-down (γ and δ) bands move towards the lower and higher BEs, respectively, as the magnetic moment per Cobalt atom decreases. The experimentally observed position of these bands do not lie exactly on the DFT-predicted lines but they show much better agreement, especially for α in Ni. This means that shift with doping is dominated by the magnetic shift, which was incorrectly predicted for Ni by VCA. On the other hand, the position of the ϵ band in Ni is not well predicted. As this band overlaps with many other bands (see Appendix B), it is difficult to determine whether this difference is significant.

V. ELECTRONIC BAND STRUCTURE IN PARAMAGNETIC STATE

Next, we study the evolution with temperature from the ferromagnetic to the paramagnetic state. Figures 4(a)–4(d)
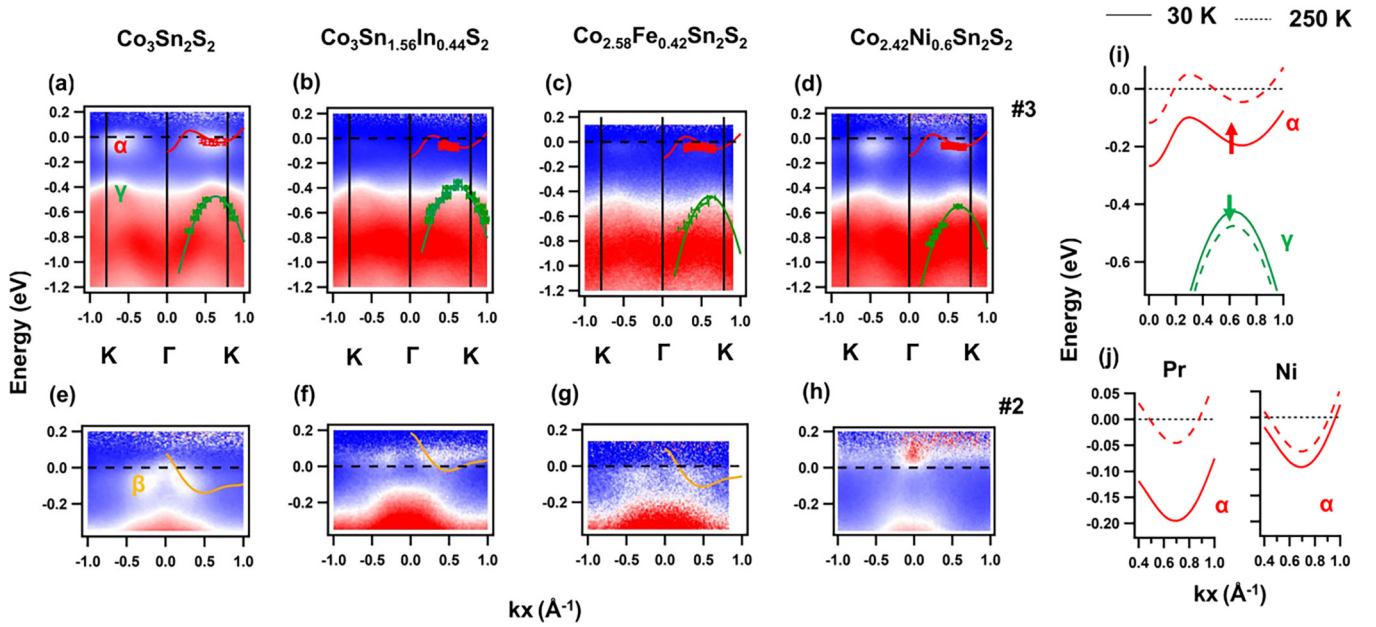
FIG. 4. (a)–(d) ARPES images collected at 250 K along cut No. 3 [as defined in Fig. 2(a)] by using 117 eV LH light of $Co_3Sn_2S_2$, $Co_3Sn_{1.56}In_{0.44}S_2$, $Co_{2.58}Fe_{0.42}Sn_2S_2$, and $Co_{2.4}Ni_{0.6}Sn_2S_2$ respectively. α and γ bands are marked by red and green colors. (e)–(h) Same along cut No. 2 (β band). These images are divided by Fermi-Dirac distribution at 250 K to highlight the unoccupied region above E_F. The overlaid lines are the same as shown in Fig. 2 but they are shifted to match with the 250 K data. (i) Comparison of the models of α and γ bands for temperature 30 K (solid line) and 250 K (dotted line). (j) Comparison of the model of α band in $Co_3Sn_2S_2$ (left) and $Co_{2.4}Ni_{0.6}Sn_2S_2$ (right) for temperature 30 K (solid line) and 250 K (dotted line).

present ARPES images along cut No. 3, in the same conditions as Fig. 2, albeit at 250 K instead of 30 K, where all compounds are in a paramagnetic state. In these images, one can notice that the separation becomes larger between the γ and α bands, spin down and up, respectively, as compared to 30 K. In Fig. 4(i), we compare the models observed for γ and α bands at 30 K (solid lines) and 250 K (dotted lines). When the magnetic splitting closes, the spin-up band moves up and the spin-down band down, enlarging the gap between them. This larger gap between γ and α is then a direct consequence of the magnetic transition. We can also see that at 250 K, when this magnetic shift is removed, the α band in $Co_{2.4}Ni_{0.6}Sn_2S_2$ [Fig. 4(d)] lies at higher BE in comparison to its position in $Co_3Sn_2S_2$ [Fig. 4(a)], as expected from electron doping. When the magnetic shift is present, as sketched in Fig. 4(j), the shift appears differently due to the reduced magnetic splitting in the Ni-doped sample in comparison to the pristine compound.

In Figs. 4(e)–4(h), images are shown at 250K along cut No. 2. The β band similarly exhibits a shift towards E_F as temperature rises to 250 K in the pristine and hole-doped compounds [Figs. 4(e)–4(g)]. In the Ni-doped compound [Fig. 4(h)], β is still unclear, as it was at 30 K, but the spectral weight we observed at 30 K just below E_F at $k_x = 0.0$ Å^{-1} is now shifted above E_F. This reveals the structure of the bands just above E_F that cannot be observed in the other compounds.

We summarize in Fig. 5(a) the positions of the α, β, and γ bands as a function of doping at 250 K, with dotted line representing their values in the paramagnetic state obtained from VCA calculations. The VCA calculation predicts a smooth evolution and this is indeed the qualitative trend. For Ni, there is a clear electron shift for γ and α bands. We again find a difference between Fe and In positions, Fe falling roughly

between pristine and In. However, the experimental value for β found in $Co_3Sn_{1.56}In_{0.44}S_2$ lies clearly above this calculated line, suggesting a deviation for the near E_F states with respect to the calculation. Indeed, even at the VCA level, this part of the band structure is not rigidly shifted (the shift is nonlinear for β at $x = 0.6$). The shape of the band also slightly changes (see Appendix D). This is probably due to the influence of the hybridized Sn states, and the In doping might amplify the effect. We also note that we neglected here structural evolution, which is not negligible for In [24].

We plot in Fig. 5(b) the energy difference between the PM and FM states for the α, β, and γ bands with respect to the magnetic moment. This difference is positive for the α and β bands (spin up) and negative for the γ band (spin down), as expected from the different spin direction. In addition, the amplitude of the shift is different for the three bands and it shows reasonable agreement with VCA calculations. The larger FM-PM difference (experiment) for the β band in comparison to α and γ bands highlights that the Weyl loop is particularly sensitive to magnetic strength compared to the rest of the electronic structure.

To better visualize the relative importance of doping-induced and magnetic-induced shifts, we plot in Fig. 5(c) the calculated and experimental positions for β as a function of doping in magnetic and nonmagnetic states. The magnetic splitting reduces from 0.35 eV to 0.2 eV between $x = 0$ and $x = 0.4$, while β shifts towards E_F by 0.05 eV in the PM state and 0.15 eV for the up band in the ferromagnetic state. The magnetic shift is then the dominant effect. In our experiment, the magnetic splitting cannot be determined directly, as the two spin directions of one band are never observed simultaneously. Near E_F, one spin direction is unoccupied, above
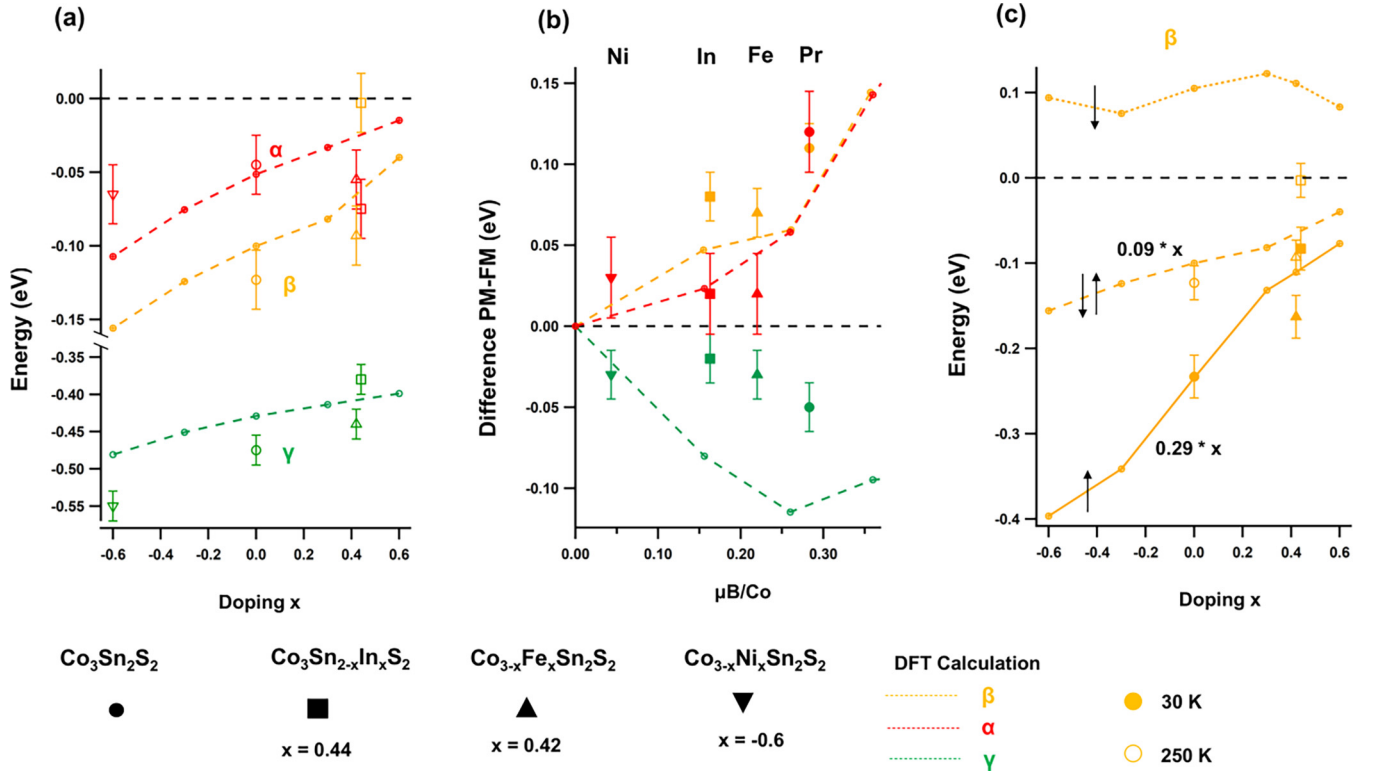
FIG. 5. (a) Position of the α (red), β (orange), and γ (green) bands as a function of hole ($x > 0$) and electron ($x < 0$) doping at 250 K obtained from the data shown in Fig. 4. Dotted lines represent their DFT-predicted value obtained from VCA calculations in paramagnetic state. (b) Energy difference of the α, β, and γ band positions between paramagnetic state (PM) at 250 K and ferromagnetic state (FM) at 30 K with respect to the magnetic moment per Cobalt atom obtained from the Fig. 1(k). (c) β band position for different dopings, where empty and filled symbols correspond to data at 250 K and 30 K, respectively. The center dashed line is the β band position for paramagnetic calculation. This splits into spin-up and spin-down bands in ferromagnetic calculations and this spin orientation is marked by up and down black arrows. Doping dependent evolution of the β band in PM (0.09) and FM state (0.29) is obtained by linear fitting to the paramagnetic and spin-up calculations, respectively, and written in (c).

E_F, and therefore not observed. At higher BE, the two spin directions overlap too strongly to be resolved. The energy difference between PM state at 250 K and FM state at 30 K of each band gives an indication of the reduction of magnetic splitting, but also depends on the position of E_F within the band, which depends on details of the semimetallic structure.

VI. DISCUSSION

One of the remarkable features of $Co_3Sn_2S_2$ is the high value of AHC. It is believed to arise from the proximity of the WPs to the Fermi level. According to Kubo formula,

$\sigma_{xy} = \frac{e^2}{h} \sum_n \int_{BZ} \frac{d^3k}{(2\pi)^2} b^z_{nk} f(E_{nk} - \mu)$, strong Berry curvature (b^z_{nk}) around the nodal ring should contribute significantly to the AHC [13]. Here, $f(E_{nk} - \mu)$ is the Fermi Dirac distribution, where μ represents Fermi level, which can be tuned by doping. However, dopants not only modify the AHC by changing the Fermi level (intrinsic factor) but also due to scattering effects (extrinsic factor). The relative magnitude of these two contributions is still debated [17,21,26].

In this situation, our doping-dependent ARPES study of the electronic structure of $Co_3Sn_2S_2$ allows us to directly locate quantitatively the main bands as a function of doping with respect to the Weyl loop [5]. The Weyl loop is formed by the crossing of two inverted bands near E_F—the β band studied

in this paper gives an example of these two bands close to a crossing, which takes place just above E_F. In Fig. 6(a), we show the position of the loop around L in the k_y - k_z plane, as calculated by DFT similarly to previous studies [14,27]. The color code indicates the energy position of the crossing with respect to E_F. The SOC opens a gap of $\simeq 60$ meV everywhere [27] except at the WPs indicated by asterisks. The band structures calculated at $k_z = 0$ (red line) and $k_z = 1/3$ (green line) along k_y are indicated in Fig. 6(b), with the renormalization of 1.4 indicated by ARPES, with and without SOC (thick and thin lines, respectively). The cuts we considered in Fig. 2 are perpendicular to this k_y direction at positions indicated on the figure. The typical position of E_F observed for the different dopings are indicated on this plot.

From this plot, we see that the Fermi level in the pristine compound lies just below the position of the Weyl crossing at $k_z = 0$ and above the Weyl crossing at $k_z = 1/3$. With hole doping, the Fermi level will move to the energy region where the Weyl crossings occur for $k_z = 1/3$ rather than around L (green dispersion in Fig. 6). This is where the crossing takes place, the lowest energy, and where the SOC gap is the largest. It was argued that strong Berry curvature around the nodal ring should contribute significantly to the AHC in these conditions [9]. Indeed, previous studies have found that the maximum of AHC occurs for a small hole doping. The
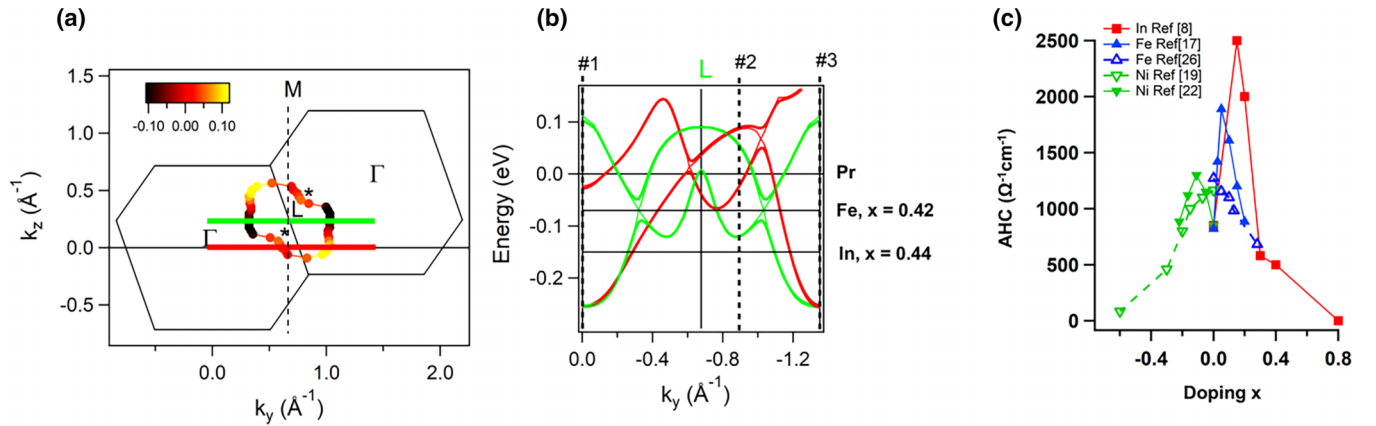
FIG. 6. (a) Position of the Weyl loop in the k_y versus k_z plane, as obtained from DFT calculation. The black lines indicate the 3D BZ, the points the position of the crossing between the two bands forming the Weyl loop, and the color corresponds to the energy position of the crossing. (b) Band dispersion along Γ - M at $k_z = 0$ (red) and $k_z = 1/3$ (green) (thin line without SOC and thick line with SOC). E_F for the Fe and In substitutions considered in this paper at 30 K are indicated. The cuts of Fig. 2 are perpendicular to k_y at positions indicated by the dotted lines. (c) AHC as a function of doping reproduced from previous results in the literature for In [8], Fe (filled up triangle [17], empty up triangle [26]) and Ni (filled down triangle [22], empty down headed triangle [19]).

previous results by Shen *et al.* for Fe [17] and Zhou *et al.* for In [8] are reproduced in Fig. 6(c). Although the shape of the two hole-doped cases is similar, the peak occurs at different doping values $x = 0.05$ in the case of Fe and $x = 0.15$ in the case of In. From our ARPES study, we directly observe a difference in the shifting amount of Weyl band β between the In (0.15 eV /0.12 eV) and Fe (0.07 eV/0.03 eV) doping at 30 K/250 K, despite the nearly similar ($\simeq 0.4$) doping level. It suggests that the effective doping obtained from Fe is half that of In. If this was the reason for the different maximum of AHC, we would rather expect to find the Fe maximum at twice the value of In. Therefore, the increase of the AHC is probably due to extrinsic contribution, as was indeed suggested [20]. Fe atoms, going to the kagome layer of Co atoms, enhances asymmetric scattering of the conduction electrons, which is an extrinsic factor to generate AHC [20] much more efficiently than for In. The maximum value of AHC itself could depend on the details of the electronic structure at one particular doping.

For Ni doping, the AHC measured by Shen *et al.* [21] also increases slightly with small doping (it shows a maximum at $x = 0.056$) and then decreases. This peak was not as clear in a previous measurement [18]. This seems to confirm the extrinsic origin of this increase, irrespective of the E_F position. A recent work has also elaborated that the AHC evolution of $Co_3Sn_2S_2$ by different (Fe and Ni) dopings depend on crystal growth method [26].

VII. SUMMARY

Our comparative study of hole- ($Co_3Sn_{1.56}In_{0.44}S_2$, $Co_{2.58}Fe_{0.42}Sn_2S_2$) and electron- ($Co_{2.4}Ni_{0.6}Sn_2S_2$) doped samples finds that the T_c and magnetic moment of $Co_3Sn_2S_2$ is suppressed by all forms of dopings. However, although the number of added holes is nearly the same between the two hole substitutions (In and Fe), the T_c and magnetic moment evolve differently. Furthermore, the Weyl band β shift towards E_F with respect to pristine is $\simeq 0.15$ eV and 0.07 eV,

respectively, by In and Fe doping in ferromagnetic state at 30 K. This shift reduces to $\simeq 0.12$ eV and 0.03 eV in the paramagnetic state at 250 K. These differences show that the dopant sites influence the type of electron transfer, which appears reduced for Fe. In the case of Ni, it is more difficult to evaluate the effective doping because the β band is not clear. On the other hand, our study reveals bands lying close above E_F, which are occupied by the added electrons. This complements our knowledge of the near E_F structure of this material. Our investigation confirms that the DFT calculation gives a good starting point to describe the electronic structure but we also noted some discrepancies about the near E_F states, for example, the position of β in the PM state for In or of the pockets above E_F revealed by Ni doping. Although rather small, these deviations can have significant consequences for the shallow pockets governing the properties in this semimetallic structure.

In this ARPES investigation, we have given particular attention to representative bands of the spin-up and spin-down directions. This has clarified how doping and magnetism influence their relative positions. We find a shift of $\simeq 0.29 \times x$ eV in the magnetic state for states near E_F and $\simeq 0.09 \times x$ eV in the paramagnetic state (here, x is the doping concentration). This complements the information already published on the pristine compound [10,11,14,15,27,28], which focused essentially on the spin up near E_F states. It is quite remarkable that DFT predictions describe rather well the magnetic transition. This contrasts with the situation in other ferromagnetic systems, like Fe_3GeTe_2, where the magnetic splitting does not vanish clearly at T_c [29,30]. This suggests an itinerant origin of magnetism with relatively small correlation effects in $Co_3Sn_2S_2$.
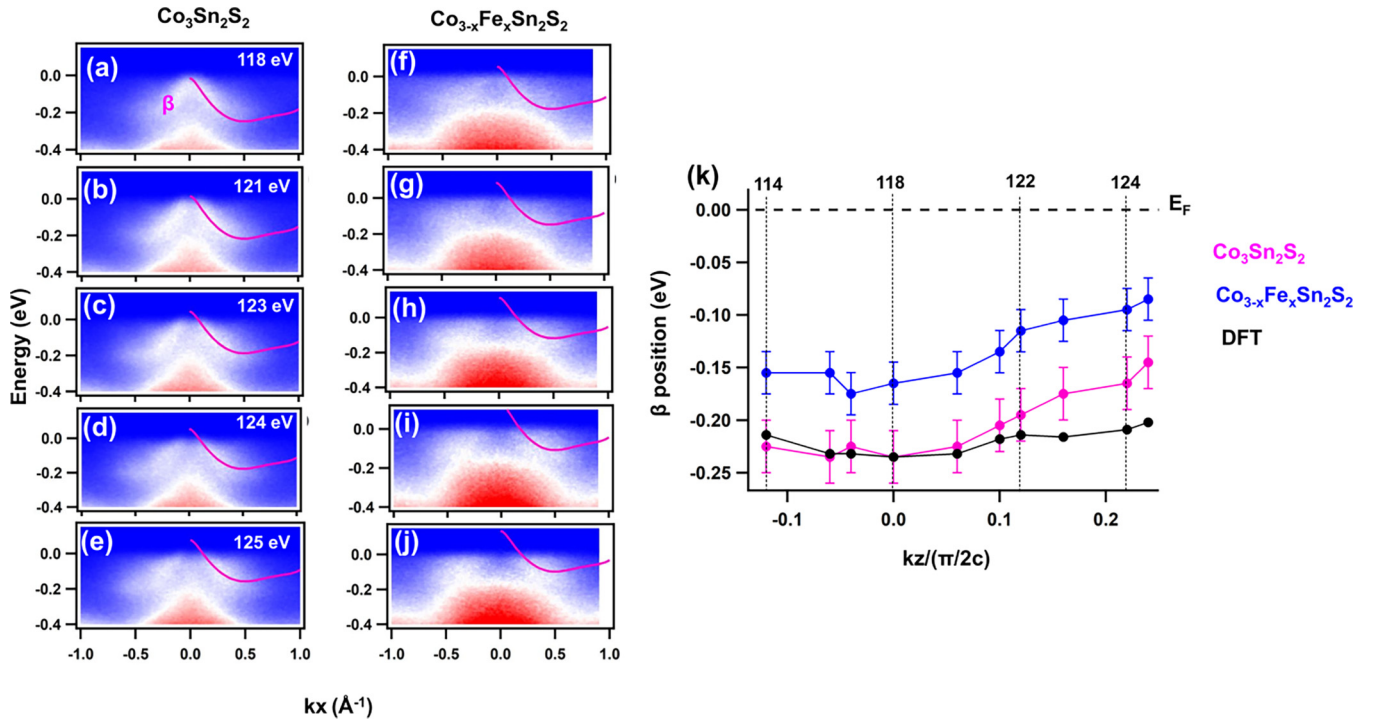
FIG. 7. (a), (f); (b), (g); (c), (h); (d), (i); (e), (j) ARPES images displaying the β band dispersion for LH polarization at 30 K and photon energies 118 eV, 121 eV, 123 eV, 124 eV, and 125 eV for $Co_3Sn_2S_2$ and $Co_{2.58}Fe_{0.42}Sn_2S_2$, respectively, where DFT-predicted β band (magenta color) is overlaid in these images. (k) Bottom part of the β band position observed in $Co_3Sn_2S_2$ (magenta) and $Co_{2.58}Fe_{0.42}Sn_2S_2$ (blue) as a function of k_z normalized by $\pi/2c$ factor, where c is the distance between planes in $Co_3Sn_2S_2$. The black data points represent DFT-predicted actual k_z dispersion of the β band in pristine compound.

APPENDIX

1. Estimation of the value of k_z at 117eV

In photoemission, the dispersion perpendicular to the plane direction (k_z) can be mapped by varying the photon energy [31]. One can convert the photon energy to the k_z value by using formula $k_z = \sqrt{\frac{2m}{\hbar^2}}\sqrt{(h\nu - \phi - E_B)\cos^2\theta + V_0}$, where ϕ, E_B, θ, and V_0 correspond to work function, BE of photoelectron, emission angle of photoelectron with respect to the sample normal, and inner potential of the sample, respectively. V_0 is estimated from the periodicity of the observed dispersion. We found that the value of V_0=11eV allows a good description of the experimental periodicity, which is in agreement with earlier works [10]. Figures 7(a)–7(e) show the β band dispersion for the photon energy range 118 eV–125 eV at 30 K. We find that the β band position is minimum near 117 eV and shifts towards E_F with increasing photon energy. As it does not drastically change its shape, we follow its position by shifting the DFT dispersion at k_z=0 (after renormalization by a factor of 1.4, see next section). This behavior, reported in Fig. 7(k), is in reasonably good correspondence with the DFT calculation for the β band. This allows us to assign a value k_z=0 to our experiment at 117 eV. Note that the well-defined k_z variation of the β band implies it is a bulk band.

2. Comparison to band-structure calculations

In this section, we compare the bands α, β, γ, δ, and ϵ described in the text with respect to the DFT calculation.

Figure 8(a) displays the BZ boundaries expected when the normal incidence corresponds to the k_z=0 (Γ point). The black hexagon corresponds to the 2D BZ of the kagome plane, with ΓK and ΓM as high-symmetry directions. In color, we represent the cut of the 3D BZ at different k_z values: red for $k_z = 0.0$, blue for $k_z = 2/3\pi/c$, and green for $k_z = -2/3\pi/c$. Indeed, adjacent BZs have different k_z values with respect to central BZ in the rhomboedral structure (see stacking in Fig. 6). The three cuts we consider in the main text are indicated and the ARPES intensity plots taken for the pristine compound at 30 K using LH polarized light of 117 eV along these cuts are presented in Figs. 8(b)–8(d), respectively. The points extracted from the images are indicated. DFT calculated bands for ferromagnetic phase (normalized by a factor of 1.4) are superimposed in these images, where violet and maroon colors represent spin-up and spin-down bands, respectively. Along cut 1, the α (red) and δ (black) bands are well reconciled with the near E_F spin-up and spin-down bands, respectively. Similarly, the β (orange) and α bands along cuts 2 and 3 exhibit a reasonable matching with the DFT prediction. The intensity patch of ϵ (blue) band falls in an energy window where more than one band are present.

3. Surface state behind the β band

Figures 9(a)–9(c) show the FS of $Co_3Sn_2S_2$ taken at 30 K by using LH, circular left (CL), and circular right (CR) polarized light of photon energy 117 eV. ARPES intensity plots along cut 1 are displayed in Figs. 9(d)–(9)(f) respectively. In
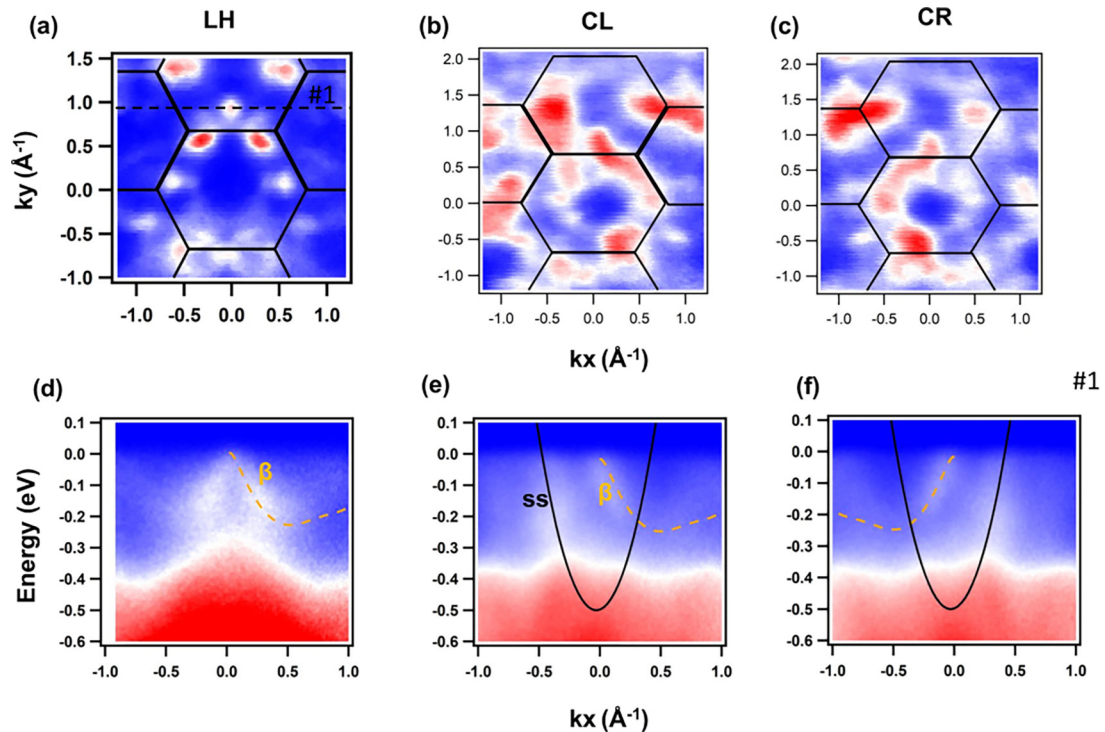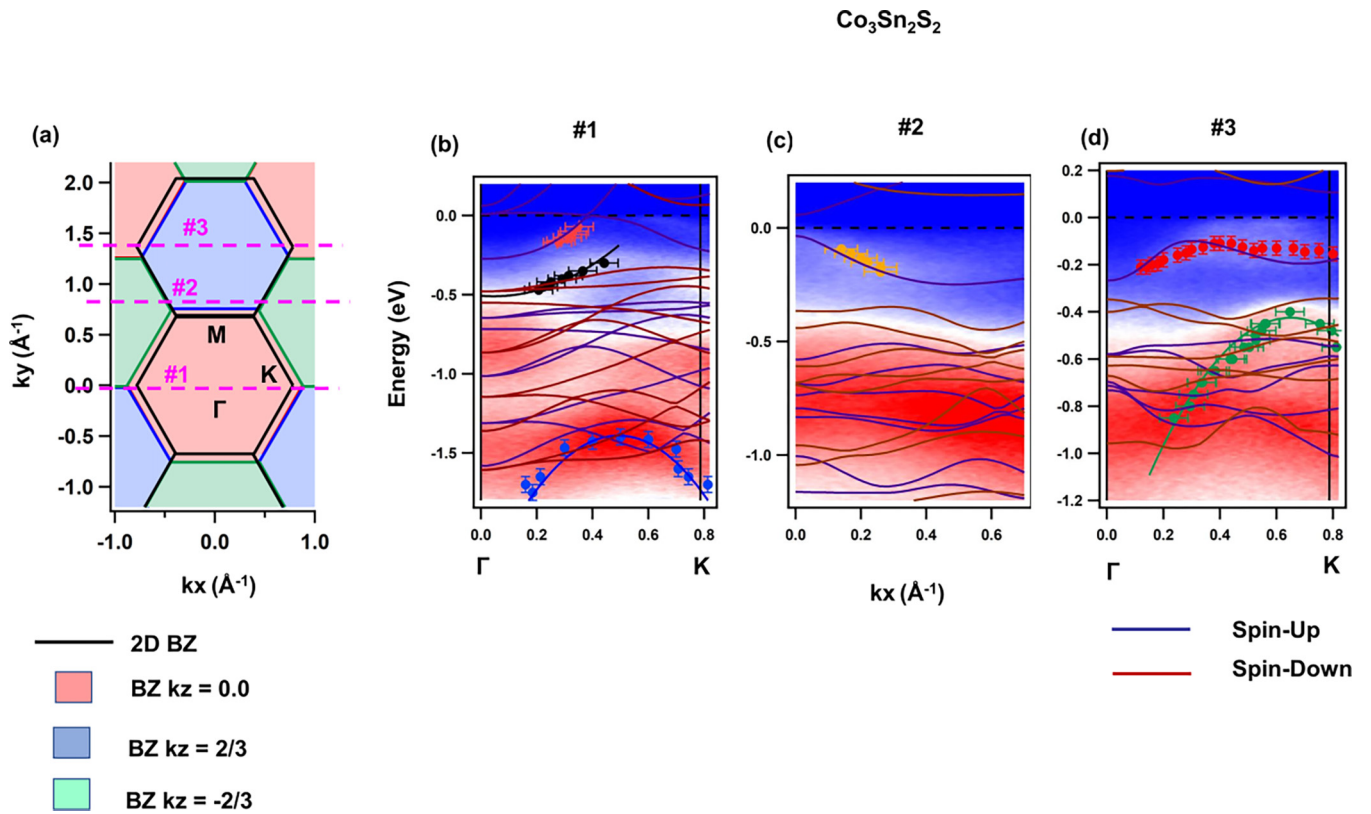
Co$_3$Sn$_2$S$_2$

FIG. 8. (a) BZ boundary of Co$_3$Sn$_2$S$_2$ in k_x and k_y planes, where red, blue, and green color-filled areas correspond to the BZ boundary k_z value = 0.0, $2/3\pi/c$, and $-2/3\pi/c$, respectively. (b)–(d) ARPES images of Co$_3$Sn$_2$S$_2$ taken at 30 K using LH polarized light of 117 eV along the cuts 1–3, respectively. Violet and marron colors represent spin-up and spin-down bands, respectively, obtained from the DFT calculation for ferromagnetic phase along the respective cuts. These bands are renormalized by a factor of 1.4 to match with experimental bands.

FIG. 9. Fermi Surface of Co$_3$Sn$_2$S$_2$ taken at 30 K by using LH (a), CL (b), and CR (c) polarized light of photon energy 117 eV. (d)–(f) ARPES images along cut 1 taken from (a)–(c), respectively. Here, SS denotes surface state band and β is a bulk band.
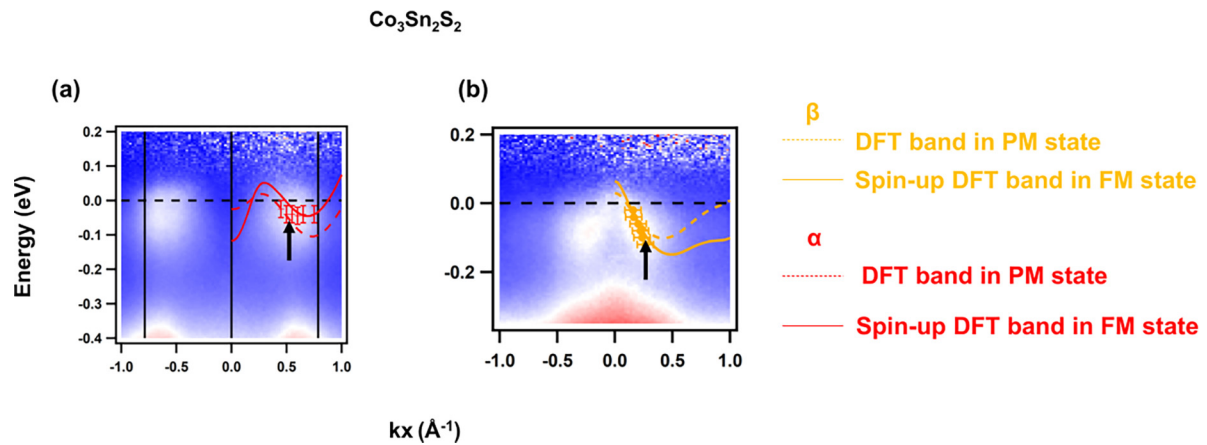
FIG. 10. ARPES image of $Co_3Sn_2S_2$ along cuts 3 (a) and 2 (b) taken at 250 K by using LH polarized light of 117 eV. These images are divided by Fermi-Dirac distribution at 250 K to highlight the unoccupied region above E_F. In these images, red and orange solid and dotted lines represent DFT predicted α and β bands (renormalized by 1.4) calculated for FM and PM states, respectively. Black arrow indicates k position of the α/β band which is used to estimate their energy values for experimental (from FM DFT band) and theoretical (from PM DFT band) values in Fig. 5(a).

LH polarization, mainly the β band is visible but in circular polarization we can see another electron like band is present just behind the β band which is denoted as surface state band (SS). No such electronlike band is present in bulk DFT calculation along this cut, so most possibly this is a surface related band. The β and SS bands show opposite responses to circularly polarized light, i.e., left and right branches of the β and SS are more intense in CL light and vice versa in CR light.

4. Determination of α and β band position

To determine the position of bands for Fig. 3 and 5, we use the position at $k_x = 0.51$ Å^{-1} for α and $k_x = 0.35$ Å^{-1} for β, both for experiment and calculation. These k points are shown by black arrows in Figs. 10(a) and 10(b) for images taken for $Co_3Sn_2S_2$ along cuts 2 and 3 at 250 K.

The DFT-predicted bands, renormalized by 1.4, are shown for the PM state (dashed line) and for the FM state (solid line, spin up) with an upshift needed to reach the experimental position.

In Fig. 4, to describe the α and β bands at 250 K, we shift the DFT-predicted band calculated for ferromagnetic state (renormalized by 1.4) towards E_F to match with the ARPES data at 250 K. Thus, we use the same model to estimate the α band position at low T (30 K) and high T (250 K) and we can define a shift between them, independently of details of the calculation.

However, we can notice there is a slight difference in the DFT calculated band shape in FM and PM states. This shows the limit of the rigid shift approach. The sensitivity of the near E_F structures beyond a simple shift can play an important role for this semimetallic state with few carriers, but they are beyond the scope of this paper.

[1] N. P. Armitage, E. J. Mele, and A. Vishwanath, Weyl and Dirac semimetals in three-dimensional solids, Rev. Mod. Phys. **90**, 015001 (2018).

[2] S.-Y. Xu, I. Belopolski, N. Alidoust, M. Neupane, G. Bian, C. Zhang, R. Sankar, G. Chang, Z. Yuan, C.-C. Lee, S.-M. Huang, H. Zheng, J. Ma, D. S. Sanchez, B. K. Wang, A. Bansil, F. Chou, P. P. Shibayev, H. Lin, S. Jia, and M. Zahid Hasan, Discovery of a Weyl fermion semimetal and topological Fermi arcs, Science **349**, 613 (2015).

[3] S.-Y. Xu, I. Belopolski, D. S. Sanchez, C. Zhang, G. Chang, C. Guo, G. Bian, Z. Yuan, H. Lu, T.-R. Chang, P. P. Shibayev, M. L. Prokopovych, N. Alidoust, H. Zheng, C.-C. Lee, S.-M. Huang, R. Sankar, F. Chou, C.-H. Hsu, H.-T. Jeng, A. Bansil, T. Neupert, V. N. Strocov, H. Lin, S. Jia, and M. Zahid Hasan, Experimental discovery of a topological Weyl semimetal state in TaP, Sci. Adv. **1**, e1501092 (2015).

[4] I. Belopolski, P. Yu, D. S. Sanchez, Y. Ishida, T.-R. Chang, S. S. Zhang, S.-Y. Xu, H. Zheng, G. Chang, G. Bian, H.-T. Jeng, T. Kondo, H. Lin, Z. Liu, S. Shin, and M. Zahid Hasan, Signatures

of a time-reversal symmetric Weyl semimetal with only four Weyl points, Nat. Commun. **8**, 942 (2017).

[5] E. Liu, Y. Sun, N. Kumar, L. Muechler, A. Sun, L. Jiao, S.-Y. Yang, D. Liu, A. Liang, Q. Xu, J. Kroder, V. Süß, H. Borrmann, C. Shekhar, Z. Wang, C. Xi, W. Wang, W. Schnelle, S. Wirth, Y. Chen *et al.*, Giant anomalous Hall effect in a ferromagnetic kagome-lattice semimetal, Nat. Phys. **14**, 1125 (2018).

[6] W. Schnelle, A. Leithe-Jasper, H. Rosner, F. M. Schappacher, R. Pöttgen, F. Pielnhofer, and R. Weihrich, Ferromagnetic ordering and half-metallic state of $Sn_2Co_3S_2$ with the shandite-type structure, Phys. Rev. B **88**, 144404 (2013).

[7] Z. Guguchia, H. Zhou, C. N. Wang, J.-X. Yin, C. Mielke III, S. S. Tsirkin, I. Belopolski, S.-S. Zhang, T. A. Cochran, T. Neupert, R. Khasanov, A. Amato, S. Jia, M. Z. Hasan, and H. Luetkens, Multiple quantum phase transitions of different nature in the topological kagome magnet $Co_3Sn_{2-x}In_xS_2$, npj Quantum Mater. **6**, 50 (2021).

[8] H. Zhou, G. Chang, G. Wang, X. Gui, X. Xu, J.-X. Yin, Z. Guguchia, S. S. Zhang, T.-R. Chang, H. Lin, W. Xie, M.

Zahid Hasan, and S. Jia, Enhanced anomalous Hall effect in the magnetic topological semimetal $Co_3Sn_{2-x}In_xS_2$, Phys. Rev. B **101**, 125121 (2020).

[9] Y. Yanagi, J. Ikeda, K. Fujiwara, K. Nomura, A. Tsukazaki, and M.-To Suzuki, First-principles investigation of magnetic and transport properties in hole-doped shandite compounds $Co_3In_xSn_{2-x}S_2$, Phys. Rev. B **103**, 205112 (2021).

[10] D. F. Liu, A. J. Liang, E. K. Liu, Q. N. Xu, Y. W. Li, C. Chen, D. Pei, W. J. Shi, S. K. Mo, P. Dudin, T. Kim, C. Cacho, G. Li, Y. Sun, L. X. Yang, Z. K. Liu, S. S. P. Parkin, C. Felser, and Y. L. Chen, Magnetic Weyl semimetal phase in a Kagomé crystal, Science **365**, 1282 (2019).

[11] Q. Wang, Y. Xu, R. Lou, Z. Liu, M. Li, Y. Huang, D. Shen, H. Weng, S. Wang, and H. Lei, Large intrinsic anomalous Hall effect in half-metallic ferromagnet $Co_3Sn_2S_2$ with magnetic Weyl fermions, Nat. Commun. **9**, 3681 (2018).

[12] Q. Xu, E. Liu, W. Shi, L. Muechler, C. Felser, and Y. Sun, Topological surface Fermi arcs in the magnetic Weyl semimetal $Co_3Sn_2S_2$, Phys. Rev. B **97**, 235416 (2018).

[13] A. Ozawa and K. Nomura, Two-orbital effective model for magnetic Weyl semimetal in Kagome-lattice shandite, J. Phys. Soc. Jpn. **88**, 123703 (2019).

[14] I. Belopolski, T. A. Cochran, X. Liu, Z.-J. Cheng, X. P. Yang, Z. Guguchia, S. S. Tsirkin, J.-X. Yin, P. Vir, G. S. Thakur, S. S. Zhang, J. Zhang, K. Kaznatcheev, G. Cheng, G. Chang, D. Multer, N. Shumiya, M. Litskevich, E. Vescovo, T. K. Kim, C. Cacho, M. Zahid Hasan *et al.*, Signatures of Weyl Fermion Annihilation in a Correlated Kagome Magnet, Phys. Rev. Lett. **127**, 256403 (2021).

[15] D. F. Liu, Q. N. Xu, E. K. Liu, J. L. Shen, C. C. Le, Y. W. Li, D. Pei, A. J. Liang, P. Dudin, T. K. Kim, C. Cacho, Y. F. Xu, Y. Sun, L. X. Yang, Z. K. Liu, C. Felser, S. S. P. Parkin, and Y. L. Chen, Topological phase transition in a magnetic Weyl semimetal, Phys. Rev. B **104**, 205140 (2022).

[16] Z. Guguchia, J. A. T. Verezhak, D. J. Gawryluk, S. S. Tsirkin, J.-X. Yin, I. Belopolski, H. Zhou, G. Simutis, S.-S. Zhang, T. A. Cochran, G. Chang, E. Pomjakushina, L. Keller, Z. Skrzeczkowska, Q. Wang, H. C. Lei, R. Khasanov, A. Amato, S. Jia, T. Neupert *et al.*, Tunable anomalous Hall conductivity through volume-wise magnetic competition in a topological kagome magnet, Nat. Commun. **11**, 559 (2020).

[17] J. Shen, Q. Zeng, S. Zhang, H. Sun, Q. Yao, X. Xi, W. Wang, G. Wu, B. Shen, Q. Liu, and E. Liu, 33% giant anomalous Hall current driven by both intrinsic and extrinsic contributions in magnetic Weyl semimetal $Co_3Sn_2S_2$, Adv. Funct. Mater. **30**, 2000830 (2020).

[18] G. S. Thakur, P. Vir, S. N. Guin, C. Shekhar, R. Weihrich, Y. Sun, N. Kumar, and C. Felser, Intrinsic anomalous Hall effect in Ni-substituted magnetic Weyl semimetal $Co_3Sn_2S_2$, Chem. Mater. **32**, 1612 (2020).

[19] J. Corps, P. Vaqueiro, A. Aziz, R. Grau-Crespo, W. Kockelmann, J.-C. Jumas, and A. V. Powell, Interplay of metal-atom ordering, Fermi level tuning, and thermoelectric properties in cobalt shandites $Co_3M_2S_2$ (M = Sn, In), Chem. Mater. **27**, 3946 (2015).

[20] Y. Zhang and C. Uher, Magnetic and transport properties of Fe-doped Weyl semimetal $Co_3Sn_2S_2$, J. Alloy and Compounds **911**, 165089 (2022).

[21] J. Shen, Q. Yao, Q. Zeng, H. Sun, X. Xi, G. Wu, W. Wang, B. Shen, Q. Liu, and E. Liu, Local Disorder-Induced Elevation of Intrinsic Anomalous Hall Conductance in an Electron-Doped Magnetic Weyl Semimetal, Phys. Rev. Lett. **125**, 086602 (2020).

[22] J.-X. Yin, N. Shumiya, Y. Jiang, H. Zhou, G. Macam, H. O. Mohammad Sura, S. S. Zhang, Z.-J. Cheng, Z. Guguchia, Y. Li, Q. Wang, M. Litskevich, I. Belopolski, X. P. Yang, T. A. Cochran, G. Chang, Q. Zhang, Z.-Q. Huang, F.-C. Chuang, H. Lin, H. Lei, M. Zahid Hasan *et al.*, Spin-orbit quantum impurity in a topological magnet, Nat. Commun. **11**, 4415 (2020).

[23] L. Nordheim, Zur elektronentheorie der metalle. I, Ann. Phys. **401**, 607 (1931).

[24] M. A. Kassem, Y. Tabata, T. Waki, and H. Nakamura, Structure and magnetic properties of flux grown single crystals of $Co_{3-x}Fe_xSn_2S_2$ shandites, J. Solid State Chem. **233**, 8 (2016).

[25] P. Blaha, K. Schwarz, G. K. H. Madsen, D. Kvasnicka, J. Luitz, R. Laskowsk, F. Tran, L. Marks, L. Marks, WIEN2k: An Augmented Plane Wave Plus Local Orbitals Program for Calculating Crystal Properties.

[26] J. Liu, L. Ding, L. Xu, X. Li, K. Behnia, and Z. Zhu, Tuning the anomalous Nernst and Hall effects with shifting the chemical potential in Fe-dope and Ni-doped $Co_3M_2S_2$, arXiv:2303.08715 v1.

[27] D. F. Liu, E. K. Liu, Q. N. Xu, J. L. Shen, Y. W. Li, D. Pei, A. J. Liang, P. Dudin, T. K. Kim, C. Cacho, Y. F. Xu, Y. Sun, L. X. Yang, Z. K. Liu, C. Felser, S. S. P. Parkin, and Y. L. Chen, Direct observation of the spin-orbit coupling effect in magnetic Weyl semimetal $Co_3Sn_2S_2$, npj Quantum Mater. **7**, 11 (2022).

[28] A. Rossi, V. Ivanov, S. Sreedhar, A. L. Gross, Z. Shen, E. Rotenberg, A. Bostwick, C. Jozwiak, V. Taufour, S. Y. Savrasov, and I. M. Vishik, Electronic structure and topology across T_c in the magnetic Weyl semimetal $Co_3Sn_2S_2$, Phys. Rev. B **104**, 155115 (2021).

[29] Y. Zhang, H. Lu, X. Zhu, S. Tan, W. Feng, Q. Liu, W. Zhang, Q. Chen, Y. Liu, X. Luo, D. Xie, L. Luo, Z. Zhang, and X. Lai, Emergence of Kondo lattice behavior in a van der Waalsitinerant ferromagnet, Fe_3GeTe_2, Sci. Adv. **4**, eaao6791 (2018).

[30] X. Xu, Y. W. Li, S. R. Duan, S. L. Zhang, Y. J. Chen, L. Kang, A. J. Liang, C. Chen, W. Xia, Y. Xu, P. Malinowski, X. D. Xu, J.-H. Chu, G. Li, Y. F. Guo, Z. K. Liu, L. X. Yang, and Y. L. Chen, Signature for non-Stoner ferromagnetism in the van der Waals ferromagnet Fe_3GeTe_2, Phys. Rev. B **101**, 201104(R) (2020).

[31] S. Hufner, *Photoelectron Spectroscopy Principles and Applications* (Springer, 2003).